

FLARE HEATING IN STELLAR CORONAE

VINAY L. KASHYAP AND JEREMY J. DRAKE

Harvard-Smithsonian Center for Astrophysics, 60 Garden Street, Cambridge, MA 02138;
vkashyap@cfa.harvard.edu, jdrake@cfa.harvard.edu

AND

MANUEL GÜDEL AND MARC AUDARD

Laboratory for Astrophysics, Paul Scherrer Institute, Würenlingen and Villigen, 5232 Villigen PSI, Switzerland;
guedel@astro.phys.ethz.ch, audard@astro.phys.ethz.ch

Received 2002 March 25; accepted 2002 August 2

ABSTRACT

An open question in the field of solar and stellar astrophysics is the source of heating that causes stellar coronae to reach temperatures of millions of degrees. One possibility is that the coronae are heated by a large number of small flares. On the Sun, flares with energies as low as those of microflares are distributed with energy as a power law of the form $(dN/dE) \propto E^{-\alpha}$, with $\alpha \approx 1.8$, and α appears to increase to values of 2.2–2.7 for flares of lower energy. If the slope exceeds the critical value of 2, then in principle the entire coronal energy input can be ascribed to flares that are increasingly less energetic but are more numerous. Previous analyses of flares in light curves of active stars have shown that this index generally is greater than 2, although it may be as low as 1.6 when strong flares alone are considered. Here we investigate the contribution of very weak flares, covering the milliflare energy range, to the coronal luminosity of low-mass active stars. We analyze *Extreme Ultraviolet Explorer*/Deep Survey events data from FK Aqr, V1054 Oph, and AD Leo and conclude that in all these cases, the coronal emission is dominated by flares to such an extent that in some cases, the entire emission can be ascribed to flare heating. We have developed a new method to directly model for the first time stochastically produced flare emission, including undetectable flares, and their effects on the observed photon arrival times. We find that $\alpha_{\text{FK Aqr}} = 2.60 \pm 0.34$, $\alpha_{\text{V1054 Oph}} = 2.74 \pm 0.35$, and $\alpha_{\text{AD Leo}} = 2.03\text{--}2.32$, and the flare component accounts for a large fraction (generally greater than 50%) of the total flux.

Subject headings: methods: data analysis — methods: statistical — stars: coronae — stars: flare — stars: late-type — X-rays: stars

1. INTRODUCTION

The source of heating of solar and stellar coronae still eludes understanding, even after decades of study (e.g., Schrijver et al. 1999). Despite significant evidence that magnetic activity is the prime driver for transferring energy into the corona, the mechanism by which this transfer occurs is not established in the case of either the Sun or other stars (see, e.g., Rosner, Golub, & Vaiana 1985; Narain & Ulmschneider 1996). Numerous heating mechanisms, such as acoustic wave dissipation (Stepien & Ulmschneider 1989), Alfvén wave dissipation (Cheng, Doschek, Feldman 1979; Narain & Ulmschneider 1990), and magnetic reconnection phenomena (Parker 1988; Lu & Hamilton 1991), have been proposed, all of which might play some role in the overall heating.

Recent work in the solar case has lent strong credence to the possibility of coronal heating being dominated by small-scale explosive events suggestive of Parker’s nanoflare model, which is based on magnetic reconnections releasing energies $\sim 10^{24}$ ergs event⁻¹. It has been well known that solar microflares and milliflares¹ are distributed in number

as power laws of their energy output (Lin et al. 1984; Hudson 1991),

$$\frac{dN}{dE} = kE^{-\alpha}, \quad (1)$$

where E is the energy of the flare and k is a constant. This relation has been verified and extended to lower energies by various authors, but despite the near universal acceptance of the form of the function in equation (1) (e.g., Crosby, Aschwanden, & Dennis 1993; see Kopp & Poletto 1993 and Shimizu & Tsuneta 1997 for a different perspective), neither the index α nor the normalization k is well determined. For instance, $\alpha = 1.6\text{--}1.8$ in the hard X-ray (HXR) to microflare energy range and is variously measured to lie in the range 1.8–2.9 at lower energies (Shimizu 1995 [$\alpha = 1.5\text{--}1.6$]; Porter, Fontenla, & Simnett 1995 [$\alpha = 2.3$]; Krucker & Benz 1998 [$\alpha = 2.3\text{--}2.6$]; Parnell & Jupp 2000 [$\alpha = 2.0\text{--}2.6$]; Aschwanden et al. 2000 [$\alpha = 1.8$]; Winebarger et al. 2002 [$\alpha = 2.9 \pm 0.1$]; Veronig et al. 2002 [$\alpha = 2.03 \pm 0.09$]). Recently, Aschwanden & Parnell (2002) have used scaling laws based on energy balance arguments to conclude that α must be ~ 1.6 on the Sun. The precise value of α is of considerable interest, because if the power law is steep enough ($\alpha > 2$), then in principle a multitude of small impulsive events would be sufficient to account for the energy output of the entire corona.

Here we reconsider in particular an outstanding question in stellar X-ray astronomy, which is the nature of the apparently quiescent emission from active stars: does this

¹ Because of the vast range of flare energies encountered, the energy ranges of the different flare types are not well defined. We adopt the convention (see, e.g., Aschwanden et al. 2000) that milliflares cover the range $E \sim 10^{29}\text{--}10^{32}$ ergs, microflares $E \sim 10^{26}\text{--}10^{29}$ ergs, and nanoflares $E \sim 10^{23}\text{--}10^{26}$ ergs. We consider all events down to the microflare regime to be “normal” X-ray flare events, with similar origin, parameters, and effects, except for the differences in energy deposition.

emission actually arise from a superposition of a multitude of impulsive events (such as milliflares and microflares) or from truly quiescent plasma? Previous work based on detecting flares in EUV data (see, e.g., Audard et al. 2000) suggests that flare contribution is indeed an important factor. Further, correlations of quiescent X-ray flux with time-averaged *U*-band flare flux (Skumanich 1985; Doyle & Butler 1985) and the synchrotron radio luminosity (Güdel & Benz 1993), together with the similar correlations found in the solar case (Benz & Güdel 1994), strongly suggest a link between the apparently quiescent emission and flares. In addition, spectroscopic evidence for high-temperature plasma ($T \gtrsim 10^7$ K) during the quiescent phase (Butler et al. 1986; Kashyap et al. 1994; Drake 1996; Güdel et al. 1997; Güdel 1997) indicates that this quiescent emission could in fact be very similar to flare emission in origin. Thus, apparently quiescent coronae of active stars could be composed of a continuum of small unresolved flares, presumably distributed as power laws analogous to the Sun. This view is also supported by the double-peaked differential emission measures (DEMs) that result when an ensemble of flaring hydrodynamically evolving loops are modeled on active solar analogs (Güdel et al. 1997; Güdel 1997).

The possibility of stellar coronal heating due to small flares was considered by Ambruster, Sciortino, & Golub (1987), who searched for variability in *Einstein* data of active stars and discussed the contribution of low-level flaring to heating stellar coronae. They concluded that while flaring must contribute at some level, the evidence does not justify extending the solar power-law distributions to the stellar microflare case. Later studies of ensembles of strong stellar flares seen with *EXOSAT* and the *Extreme Ultraviolet Explorer* (*EUVE*) have shown that these are distributed as power laws with index $\alpha = 1.6\text{--}1.8$ (Collura, Pasquini, & Schmitt 1988; Pallavicini, Tagliaferri, & Stella 1990; Osten & Brown 1999), thus ruling out low-intensity flares as a significant contributor to the heating budget. In contrast, using a more sensitive method to detect fainter flares (see Crawford, Jauncey, & Murdoch 1970), Robinson et al. (1995, 1999, 2001) find that for stellar chromospheric and transition region events observed with the high-speed photometer and the imaging spectrograph on the *Hubble Space Telescope* (*HST*), $\alpha \sim 1.76\text{--}2.17$ in the chromosphere of the active dMe star CN Leo, $\alpha = 2.25 \pm 0.1$ in the chromosphere of the dMe star YZ CMi, and $\alpha \sim 2.2\text{--}2.8$ in the transition region of the dM0e flare star AU Mic. (Note, however, that chromospheric and transition-region flare distributions have no known direct correspondence with the coronal case.) Applying a similar method to *EUVE*/Deep Survey (DS) data and also correcting for overlaps in flares, Audard et al. (1999) find that for solar analogs EK Dra and 47 Cas, $\alpha \approx 2.2 \pm 0.2$. This analysis was further extended by Audard et al. (2000) to a larger sample of cool stars, and they find that α ranges from 1.5 to 2.6, with the majority of the measurements having $\alpha > 2$. Similar results are obtained for AD Leo (Güdel et al. 2001, 2002).

Note that the above studies are limited to relatively large flares ($E \gtrsim 10^{31}$ ergs) because of instrument sensitivity and also because the more numerous weaker flares are harder to detect in the presence of “contamination” by other weak flares. Thus, the low-energy end of the flare distribution is subject to large uncertainties.

We have developed a new method to *model* the undetectable stellar flares and thus derive estimates of flare indices

covering the milliflare regime, as well as directly estimating the flare contribution to the observed flux. We apply this method to active low-mass stars FK Aqr, V1054 Oph, and AD Leo. The data sets used are described in § 2. The analysis method is detailed in § 3 (a glossary of the terms used is given in Appendix Table A1). The results are given in § 4 and are summarized in § 5.

2. DATA

Here we analyze data from the *EUVE* satellite’s DS photometer of three active low-mass stars.² These stars are known to have significant flare activity and do not undergo eclipses, and so they are amenable to straightforward modeling.

FK Aqr is a BY Dra-type, spectroscopic, double-lined, nonclipping, low-mass active binary (Table 1). Its flare energy output has remained steady over long intervals (8 yr; Byrne, Butler, & Lyons 1990), and optical modulation due to spot activity has been observed. Thus, it is possible that flare heating could be a significant component of coronal emission for this star. Indeed, the *EUVE*/DS light curve shows evidence of a number of flare events (Fig. 1), as well as large stochastic variability in the apparently quiescent emission.

V1054 Oph is a low-mass astrometric binary (Table 2). Previous X-ray observations with *ROSAT* have confirmed the existence of almost continuous flaring (Kellet & Tsikoudi 1999) and the existence of high-temperature plasma that is responsible for most of the intensity variations (Giampapa et al. 1996). *EUVE* data show a large number of relatively weak flare events that blend into the variations in the quiescent emission (Fig. 2). Such a data set

² The intrinsic *EUVE* time resolution is 8 ms, and this is adequate to resolve the sources even at the maximum count rate seen in our observations (3 counts s⁻¹). The *EUVE*/DS covers a useful spectral range of 52–246 Å, with a peak effective area of 28 cm⁻² at 91 Å. This wavelength range includes many lines from highly ionized Fe xviii to Fe xxiii normally found in the coronae of active stars, in addition to bound-free and free-free continua; plasma temperatures from ≈ 1 to 30 mK are thus accessible for observation.

TABLE 1
FK AQR

Parameter	Value
Other names.....	Gl 867A, HD 214479
(R.A., decl.) (J2000).....	(22 38 45.56, -20 37 16.1)
Spectral type ^a	dM2e/dM3e
Period ^a (days).....	4.08
Distance ^b (pc).....	8.64
m_V^b (mag).....	9.06
$B-V^b$	1.47
L_X^c (ergs s ⁻¹).....	1.3×10^{29}
<i>EUVE</i> /DS.....	1997 Oct 17–24 (130.7 ks)
Count rate (counts s ⁻¹).....	0.36 ± 0.033
Background (counts s ⁻¹).....	~ 0.023

NOTE.—Units of right ascension are hours, minutes, and seconds, and units of declination are degrees, arcminutes, and arcseconds.

^a As in Strassmeier et al. 1993.

^b From the Hipparcos Catalog (Perryman et al. 1997).

^c In the *Einstein* energy band (0.1–4.5 keV; Dempsey et al. 1993).

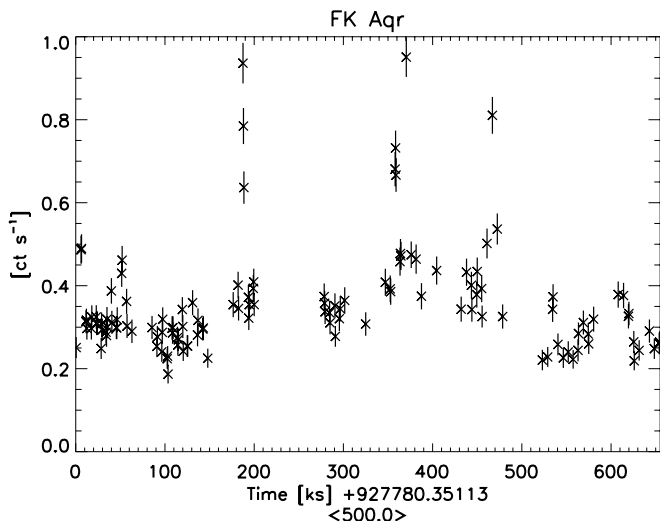


FIG. 1.—*EUVE/DS* light curve of FK Aqr. The light curve corrected for instrumental effects is shown at a bin size of 500 s. The vertical bars denote the 1σ error on the count rate. Note that there are many obvious flares visible in the light curve, in addition to a base emission that also is highly variable.

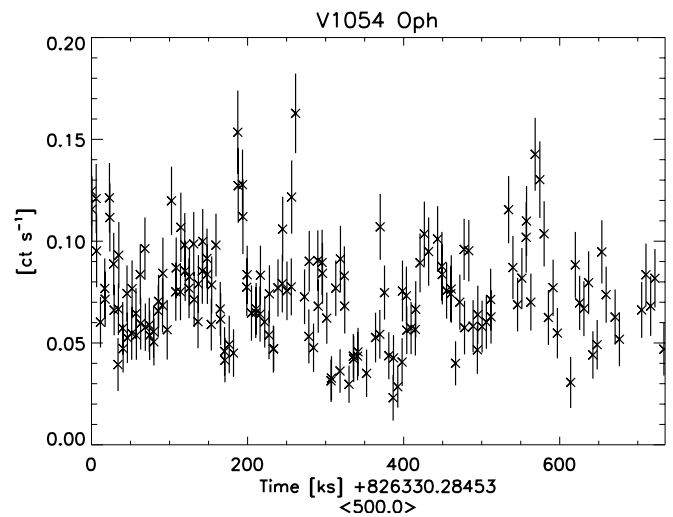


FIG. 2.—Same as Fig. 1 but for V1054 Oph. In this light curve, it is difficult to cleanly distinguish a flare event from the underlying continuous emission.

is very difficult to analyze by the traditional means of detecting and counting flares but poses no difficulty to a direct modeling approach, as is described below.

AD Leo is a well-studied low-mass single-flare star (Table 3) with a high flare rate. A long-duration exposure was obtained by Güdel et al. (2001, 2002) that shows many large flares (Fig. 3). The data were obtained in six segments, and since the first segment could not be optimally reduced and the last segment suffered from a high background, we have ignored them in this analysis and have concentrated on segments 2–5. In particular, we have carried out the analysis with the data grouped into two sets, segments 2 and 3 forming one set and segments 4 and 5 forming the other. The light curves show slightly different characters in the two parts, with the former part dominated by large flares, while the latter part shows smaller identifiable flares (Fig. 3).

In our analyses (see § 3), we use the photon arrival times directly and apply the dead-time and Primbsching correc-

tions³ for the particular observation to the models (see § 3.1) over good time intervals (GTIs) defined to exclude South Atlantic Anomaly (SAA) passages and Earth blockages. That is, we process model light curves to produce a simulated set of photons and apply time windowing and statistical censoring (i.e., the instrument response in the time domain) to generate an event list that can be directly compared to the observed events. For the sake of brevity, these corrections are henceforth referred to as “instrumental” corrections. The source photons are collected over a circle of radius $4''$ surrounding the source. In all cases, $\lesssim 10\%$ of the events are estimated to be due to background photons, except in the case of V1054 Oph, in which it is estimated to be 17%.

³ Primbsching refers to the photons lost because of telemetry bandwidth and is measured by the ratio of the total counts incident in a quadrant of the detector (as determined on the spacecraft; the summed counts from all the quadrants are used to determine the instrument dead time) to the number of events telemetered to the ground (see the *EUVE* Data Products Guide for a detailed description of its origin and correction).

TABLE 2
V1054 OPH

Parameter	Value
Other names.....	Wolf 630, Gl 644, HD 152751
(R.A., decl.) (J2000).....	(16 55 28.76, -08 20 10.8)
Spectral type ^a	M3 Ve
Distance ^a (pc).....	5.73
m_V^a (mag).....	9.02
$B-V^a$	1.553
L_X^b (ergs s ⁻¹).....	5.6×10^{28}
<i>EUVE/DS</i>	1994 Jul 30–1994 Aug 8 (127.9 ks)
Count rate (counts s ⁻¹).....	0.09 ± 0.014
Background (counts s ⁻¹).....	~ 0.015

NOTE.—Units of right ascension are hours, minutes, and seconds, and units of declination are degrees, arcminutes, and arcseconds.

^a From the Hipparcos Catalog (Perryman et al. 1997).

^b In the *Einstein* energy band (0.1–4.5 keV; Dempsey et al. 1993).

TABLE 3
AD LEO

Parameter	Value
Other names.....	GJ 388, SAO 81292
(R.A., decl.) (J2000).....	(10 19 38.04, +19 52 14.2)
Spectral type ^a	M3 V
Distance ^a (pc).....	4.9
m_V^a (mag).....	9.43
$B-V^a$	1.54
L_X^b (ergs s ⁻¹).....	8.91×10^{28}
<i>EUVE/DS</i>	1999 Apr 5–14 (258.6 ks)
	1999 Apr 17–1999 May 4 (347.7 ks)
Count rate (counts s ⁻¹).....	0.47 ± 0.03 (Apr 5–14)
	0.31 ± 0.03 (Apr 17–May 4)
Background (counts s ⁻¹).....	$\sim 0.028-0.031$

^a From Audard et al. 2000.

^b In the *Einstein* energy band (0.1–4.5 keV; Dempsey et al. 1993).

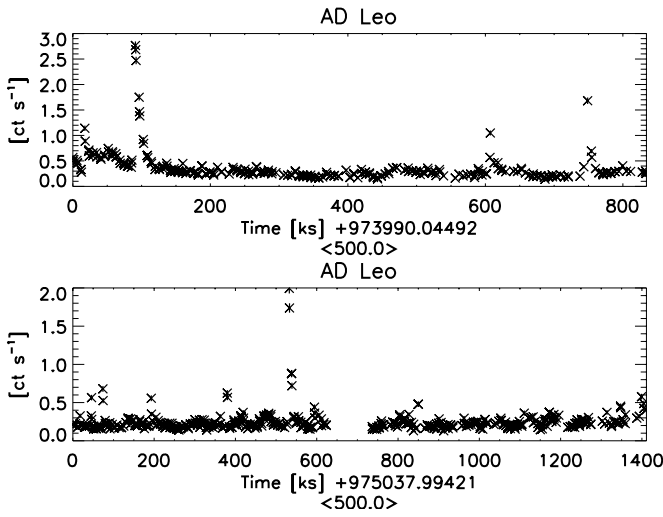


FIG. 3.—Same as Fig. 1 but for AD Leo; top panel shows segments 2 and 3 (April 5–14), and the bottom panel shows segments 4 and 5 (April 17–May 4). Many large flares are visible (especially in segment 2, which is dominated by a large flare), as well as significant variability in the apparently quiescent emission.

3. ANALYSIS

Previous attempts to determine the values of the parameters in equation (1) have concentrated on first detecting flares in the binned light curve and then fitting power-law expressions to the detected numbers. In contrast, we *assume* the reality of a power-law distribution and set up a *model* to compare with the data. This model is described in § 3.1, and the manner in which the model parameters are derived is described in § 3.2. The applicability of the method, including verification, assumptions, advantages, and disadvantages, is discussed in § 3.3.

3.1. The Model

Because flares generally occur randomly (see § 3.3.2), we cannot directly model the light curves, as it is not possible to “deconvolve” a complex light curve by specifying the location of each flare in a model (see, e.g., Fig. 2). Instead, rather than match the flare locations in detail, we carry out a fitting process wherein only the number and intensity distributions of a set of model flares are matched with the data. This is accomplished by comparing the distributions of photon arrival-time differences. The assumptions made in defining the model described below are discussed in detail in § 3.3.2.

We first generate a set of photon arrival times by simulation from a three-parameter model

$$\mathbf{M} = \{\alpha, r_F, r_C\}, \quad (2a)$$

where α is the index of the power law as in equation (1), r_F is the average count rate due to flares, and r_C is a constant component that is also expected to fully account for the background (see § 3.3.2). It is also possible to use the average *total* flux $r_T = r_F + r_C$ ($r_F < r_T$) as the defining parameter instead of r_C ,

$$\mathbf{M}' = \{\alpha, r_F, r_T\}, \quad (2b)$$

with equivalent results. The counts at time t in an interval dt , $C(t) \sim \text{Poisson}[r(t)dt]$ are Poisson-distributed according to the instantaneous rate $r(t)$. The rate $r(t)$ can be described

as due to the sum of model counts due to a flare component $f(t)$ and a nonflare component $r_C(t)$, and a correction factor $\phi(t)$ that takes into account Primbsching, dead time, and GTIs,⁴ i.e.,

$$C(t) \sim \phi(t) \text{Poisson}[r_C(t)dt + f(t)dt], \quad (3a)$$

where $r_C(t)$ is taken to be constant unless stated otherwise. The flare component $f(t)$ can in turn be written as a superposition of numerous individual flares, i.e.,

$$f(t) = \sum_{j=1}^{N_f} \Theta(t - t_j) F_j e^{-(t-t_j)/\tau}, \quad (3b)$$

where τ is the flare decay timescale,⁵ N_f are the total number of flares, F_j are the peak energy intensities of individual flares (the counts due to each flare, $c = \tau F_j$, are sampled from the distribution represented by eq. [1]), and

$$\Theta(x) = \begin{cases} 0, & x < 0, \\ 1, & x \geq 0 \end{cases}$$

is a step function to represent flare onset.

Note that not only will the placement t_j and peak intensity F_j of the flares vary for each simulation, but so will the total number of flares N_f . Within the bounds of Poisson statistics, we expect that for any given simulation, the total energy due to all the simulated flares is determined by the average expected count rate due to flares and the total duration of the observation, ΔT , i.e.,

$$\int_0^\infty dt f(t) = \sum_{j=1}^{N_f} F_j \tau = r_F \Delta T. \quad (3c)$$

Note that equation (1) is written as a function of the energy deposited by a flare E , but assuming that the observed counts due to this flare c are proportional to E (see discussion in § 3.3.2), i.e.,

$$\frac{dN}{dE} \propto \frac{dN}{dc} = \kappa c^{-\alpha} dc, \quad (4)$$

we can use the model parameter r_F to fix the normalization κ of the power law. By equating the total counts due to the flare component with the counts expected from the power-law distribution, we get

$$r_F = \frac{\int_{c_{\min}}^{c_{\max}} dc c (dN/dc)}{\Delta T}. \quad (5)$$

The upper limit in the integration is defined by requiring that all the observed counts be due to a single-model flare ($c_{\max} = \max_j \{F_j \tau\} = r_F \Delta T$); that is, no flare model may produce a flare with more counts than are observed. The lower limit in the integration is defined by requiring that each flare be assigned at least two counts (i.e., $c_{\min} = 2$; this is so that an arrival-time *difference* can be determined, even in the extreme case in which the model may have just one weak flare—see § 3.2). Thus, by carrying out the integral in

⁴ Note that $0 \leq \phi(t) \leq 1$ determines the probability that any photons are collected at time t and in particular is identically 0 outside the GTIs.

⁵ We assume τ to be fixed for purposes of simplicity. See § 3.3.2 for a discussion of cases when τ may vary.

equation (5) and rearranging the terms,

$$\kappa|_{(\alpha \neq 2)} = \frac{(2 - \alpha)r_F \Delta T}{(r_F \Delta T)^{2-\alpha} - 2^{2-\alpha}}, \quad (6a)$$

$$\kappa|_{(\alpha=2)} = \frac{r_F \Delta T}{\ln(r_F \Delta T/2)}. \quad (6b)$$

For $\alpha > 2$, this implies that if $r_F \approx r_T$, then the adopted lower limit is very close to the theoretical lower limit to the extent of the power-law distribution in order for it to account for all the observed counts (see Table 4).

In order to obtain the best values of the parameters that describe the data and a confidence range on these parameters, we carry out a forward-fitting procedure based on a Bayesian formalism (see, e.g., Loredano 1990 for a tutorial on the foundations of Bayesian probability theory); we compute the probability distribution of the model parameters given the data, which is a composite of whatever prior information we may have on the model parameter values and the likelihood of realizing the observed data for specified parameter values. That is, we derive the joint posterior probability $p(\mathbf{M}|D, I)$ of the model parameters conditional on the data,⁶

$$p(\mathbf{M}|D, I) \propto p(\alpha|I)p(r_F|I)p(r_C|I)p(D|\mathbf{M}, I), \quad (7a)$$

where D represents the data and I represents assumptions necessary to solve the problem, including the effects of instrument characteristics. The first three factors on the right-hand side of the equation are the a priori probability distribution functions of the model parameters, and the last factor, $p(D|\mathbf{M}, I)$, is the likelihood of obtaining the observed data given the model parameters. Computing the posterior probability distribution constitutes a complete solution to the inference problem for the specified model \mathbf{M} . Note that the above is a simplified form of Bayes's theorem, wherein the normalization factor $p(D|I)$ usually present on the right-hand side of the equation is ignored (e.g., Kashyap & Drake 1998; van Dyk et al. 2001). If r_T is used instead of r_C , the joint probability distribution takes the form

$$p(\mathbf{M}'|D, I) \propto p(\alpha|I)p(r_F|r_T, I)p(r_T|I)p(D|\mathbf{M}', I), \quad (7b)$$

with $p(r_F|r_T, I) = 0$ for $r_F > r_T$. In the following, we make no distinction between \mathbf{M} and \mathbf{M}' . The Bayesian formalism allows us to determine the probability distributions of each of the parameters by marginalizing, i.e., integrating over the other parameters. Thus, we can write for the probability distribution of α alone

$$p(\alpha|D, I) = \int_{r_F} dr_F \int_{r_C} dr_C p(\mathbf{M}|D, I) \quad (8)$$

and similarly for the other parameters (cf. eq. [11]).

⁶ The expression $p(x)$ represents the probability that the logical statement “ x ” is true. In particular, conditional statements are written as “ $A|B$ ”, i.e., $p(A|B)$ represents the probability that statement “ A ” is true, given that statement “ B ” is true. These statements may be generalized to include models and parameter values; as an illustrative example, $p(\{\alpha = 2.1, r_F = 0.1, r_T = 0.3\}|D, I) = 0.1$ reads as “the probability is 0.1 that $\alpha = 2.1$, $r_F = 0.1$, and $r_T = 0.3$, given the data D and supporting information I .”

3.2. The Algorithm

The problem facing the modeling process is illustrated in Figure 4, in which the light curve from the observation of FK Aqr is compared with selected simulated model light curves.⁷ It is easy to recognize that the model light curve for $\alpha = 2.5$ is the most similar in character (i.e., in the number and strength of discernible flares) to the data light curve, but clearly, the *locations* of the flares do not match. Normal fitting methods that rely on matching the expected model counts in a bin with the observed counts would fail on a problem such as this. We thus seek to employ a method that compares the interesting information between the data and the model without being misled by the obvious, although uninteresting, differences.

One method that would satisfy our requirements of simultaneously ignoring flare locations and yet be sensitive to flare numbers and intensities is to compare the distributions of photon arrival-time differences $g(\delta t)$ (where δt is the interval between consecutive counts) between the data and the model.⁸ In the absence of any variability, i.e., if the light curve is flat with expected rate r , the resulting set of δt are distributed as an exponential,

$$g(\delta t) \propto r e^{-r\delta t}. \quad (9a)$$

In the presence of variability in the expected rate, the observed distribution would be a superposition of many such distributions: if the fraction of time that a source spends at rate r_i is given as ρ_i , then

$$g(\delta t) \propto \sum_i \rho_i r_i e^{-r_i \delta t}. \quad (9b)$$

It is thus possible to distinguish between different magnitudes of variability. In particular, events generated from a model with low α (e.g., $\alpha = 1.8$, where the light curve would be dominated by a few very large flares) would result in a distribution $g(\delta t)$ that is skewed to smaller values of δt , while those from a model with large α (e.g., $\alpha = 3.0$, where the light curve would be composed of a large number of very small flares that overlap each other so finely that it would not be possible to distinguish it from a source with constant intensity) would approach the limiting case of equation (9a) above.

In Figure 5, we show the comparison between the distributions of arrival-time differences derived from the same data sets in Figure 4. The different curves can be compared using any of a number of statistical methods, such as computing the χ^2 , applying the Kolmogorov-Smirnoff test, etc. This approach succeeds in providing us with an objective measure of the “similarity” between the data sets; indeed, of the four models considered in Figures 4 and 5, the one with $\alpha = 2.5$ has the smallest χ^2 when compared with the data. Note that Figure 5 also illustrates a fundamental limitation of this method, viz., the method loses sensitivity for larger values of α , which

⁷ We emphasize that these light curves are shown only for purposes of illustration and that the analysis does not require binning the observed events.

⁸ Other methods such as computing the fractal length of the events, multiscale analyses of light curves, etc., can also be applied (see, e.g., Vlahos et al. 1995). A detailed comparison of the benefits of one method vs. another is beyond the scope of this article but note that the results we derive here are robust within the regime of applicability of the adopted method (see § 3.3).

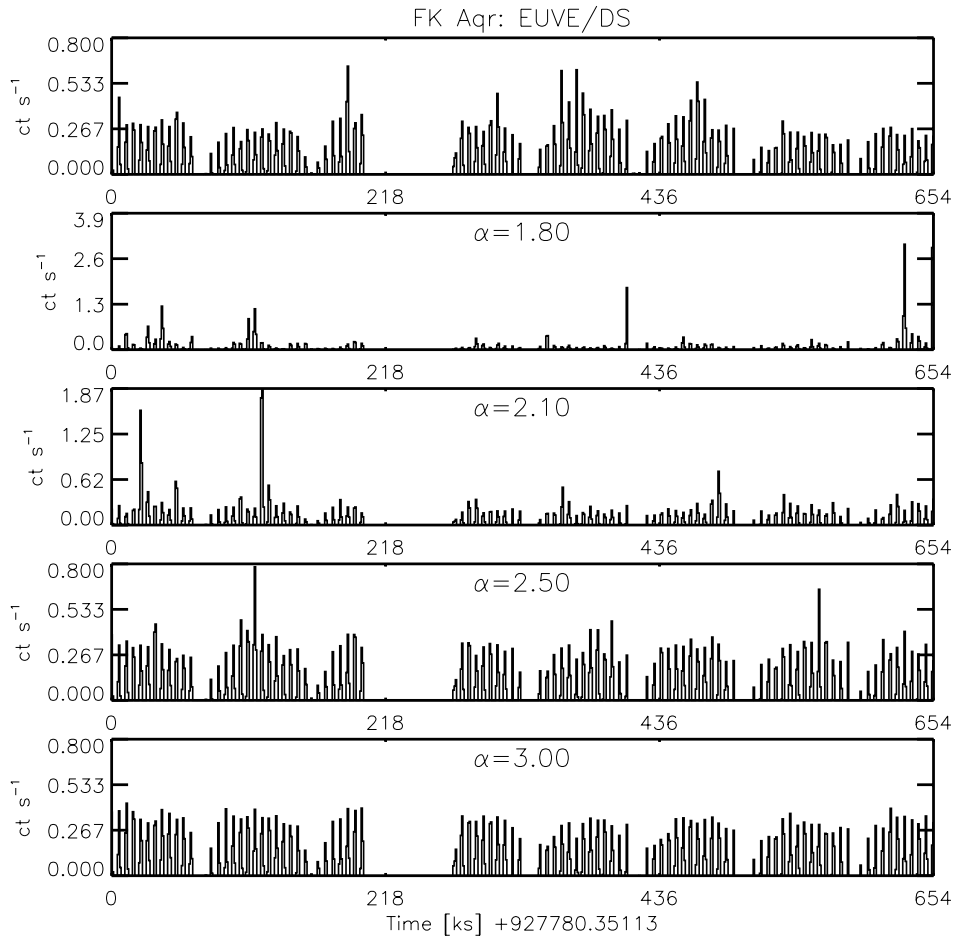


FIG. 4.—Illustrative comparison of data and model light curves. The light curve from an observation of FK Aqr is plotted in the topmost panel at a bin size of 500 s. No instrumental corrections have been applied to the data. In the bottom panels, light curves derived from simulated events for various values of the index of the power-law distribution, $\alpha = 1.8, 2.1, 2.5,$ and 3.0 , are shown at the same binning and after applying the appropriate Primbsching and dead-time corrections and GTI filtering. The model curves are computed assuming $r_C = 0$ in order to simplify the comparisons. Note the larger dynamic range in the light curves for lower α . It is apparent that the light curve for $\alpha = 2.5$ is most “similar” to the observed light curve.

may be indistinguishable from sources with a constant intensity (see § 3.3.1).

Because the model (eq. [3a]) is stochastic, we use Monte Carlo simulations to generate many realizations for each set of model parameters. The simulated distributions of arrival-time differences $g_{\text{MODEL}}(\delta t)$ are compared with the corresponding distribution derived from the data $g_{\text{DATA}}(\delta t)$ over a parameter grid. The likelihood is computed as the probability density of obtaining the observed χ^2 value for N degrees of freedom (see Eadie et al. 1971, their eq. [4.22]):

$$p(D|\mathbf{M}) = \frac{(1/2)(\chi/2)^{(N/2)-1} e^{-\chi/2}}{\Gamma(N/2)}. \quad (10)$$

The a priori probability distributions for the parameters (eq. [7a]) are taken to be noninformative, and thus flat, over the range of parameter values defining the grid. The basic steps in the algorithm we follow are outlined below:

1. From the data, derive the distribution of photon arrival-time differences, excluding the gaps in the data due to breaks in the GTIs.

2. For the specified values of model parameters \mathbf{M} (eqs. [2a] and [2b]), obtain a realization of the photon event list

over the duration of the observation. This is done by first simulating a light curve incorporating all the flare events (eq. [3b]), added to the base emission, and then deriving photon arrival times based on the instantaneous count rates.

3. Because we are to compare *EUVE/DS* event list data with simulated data, instrument effects must be taken into account. This is encoded in the factor $\phi(t)$ (see footnote 4). We apply Primbsching and dead-time corrections by discarding photons with probability $1 - \phi(t)$ [i.e., sample a random number z from a uniform distribution over the interval $(0, 1)$ and discard the photon at time t if $z > \phi(t)$]. The retained set of events is identical in its instrumental characteristics to the observed data.

4. From this set of simulated photon arrival times, derive the model distribution of arrival-time differences over a binning that *maximizes* the reduced χ^2 .⁹

⁹ We do not know the optimal binning for $g(\delta t)$ a priori. The binning must be chosen such that differences between the two distributions being compared are highlighted to best advantage, at a scale that is determined by the data sets themselves. Because the total number of photons in the data sets being compared are approximately the same, very coarse binnings and very fine binnings both produce low values of the reduced χ^2 , and we adopt as the optimal binning that which maximizes this value.

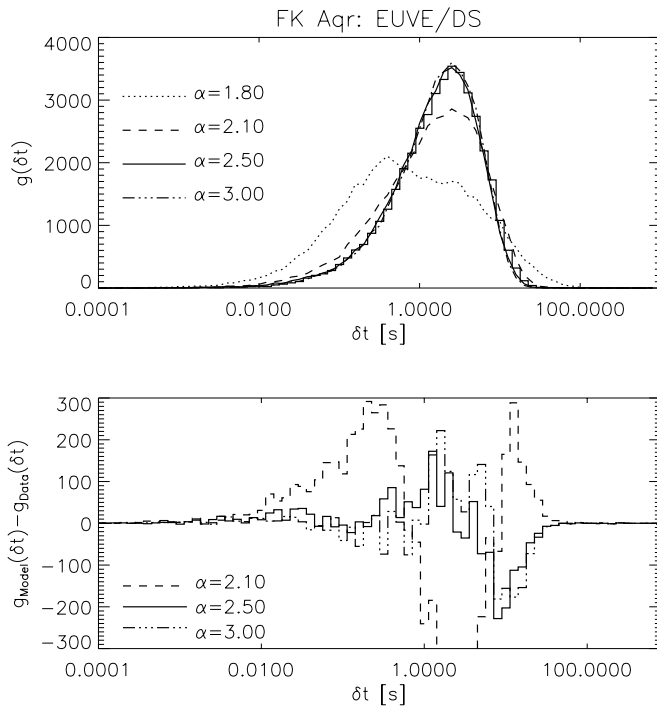


FIG. 5.—Comparison of distributions of arrival-time differences between the data and model. Note that the x -axis is in log scale. The top plot shows the full distributions $g(\delta t)$ for the data (stepped curve), $\alpha = 1.8$ (dotted curve), $\alpha = 2.1$ (dashed curve), $\alpha = 2.5$ (solid curve), and $\alpha = 3.0$ (dash-dotted curve). The models used are the same as in Fig. 4. It is apparent that the first two models are bad fits to the data. A more detailed analysis is required to select between the last two models. In order to highlight the differences in the distributions near their peaks, these differences are shown in the bottom plot, where the differences between the model and the data distributions are plotted for $\alpha = 2.1$ (dashed line), $\alpha = 2.5$ (solid line), and $\alpha = 3.0$ (dash-dotted line). A comparison of the χ^2 values indicates that $\alpha = 2.5$ is a significantly better fit to the data than $\alpha = 3$ ($\chi^2 \approx 465$ and 490 , respectively).

5. Compute the likelihood as in equation (10) and the a posteriori probability at the specified grid point as in equation (7a). Note that the number thus obtained is not normalized and so must not be used to compare, for example, the relative probabilities of different types of models.

In practice, the above algorithm must be enhanced by some additional steps. For instance, the likelihood can be artificially reduced if a large model flare is fortuitously located coincident with large dead time. We therefore shift the Primbsching and dead-time corrections by a random interval and recompute the arrival times. This is mathematically equivalent to shifting the simulated events but is done in this fashion because of the lower computational cost. Typically, three such shifts are carried out for each simulated light curve, and the best comparison is chosen. In addition, in order to derive a robust estimator, we perform ≈ 15 – 20 simulations for each M (or M') and adopt the median value of the set as the final value of $p(M|D, I)$. The grid of model parameters is chosen such that α is explored over the useful range of the algorithm (1.5, ..., 3.0; see § 3.3.1), r_F in a range within 3σ of the average count rate, and r_C and r_F ranges from ≈ 0 to the average count rate. There are typically ~ 15 grid points for each parameter.

The probability distribution along any of the axes is then obtained by summing over the other axes and normalizing,

e.g.,

$$p(\alpha|D, I) = \frac{\sum_{r_F} \sum_{r_C} p(M|D, I)}{\sum_{\alpha} \sum_{r_F} \sum_{r_C} p(M|D, I)}. \quad (11)$$

The derived probability distributions can be summarized by their means and variances,¹⁰ e.g.,

$$\bar{\alpha} = \frac{\sum_{\alpha} \alpha p(\alpha|D, I)}{\sum_{\alpha} p(\alpha|D, I)}, \quad (12a)$$

$$\text{var}(\alpha) = \bar{\alpha}^2 - (\bar{\alpha})^2. \quad (12b)$$

3.3. Applicability

As was demonstrated above (§ 3.2; Figs. 4 and 5), the distributions of arrival-time differences $g(\delta t)$ provide an objective means to compare event lists that are dominated by stochastic events. Here, we verify that the algorithm gives reasonable results by creating simulated data sets and obtaining best-fit values for them (§ 3.3.1), then discuss the effects of some of the assumptions we have made in formulating the problem (§ 3.3.2) and detail the advantages and disadvantages of the adopted method (§ 3.3.3).

3.3.1. Verification

We show here that the algorithm works as expected by simulating well-defined data sets and then “fitting” to them. We generated flare models with specific values of α (labeled α_{TRUE}) ranging from 1.5 to 3 and, for the sake of simplicity, held $r_F = 0.5$ counts s^{-1} and $r_C = 0.1$ counts s^{-1} . Simulations were carried out over a time interval $\Delta T = 100$ ks and assuming a fixed flare decay timescale of $\tau = 3$ ks. These values were chosen as being typical of *EUVE/DS* observations. The data sets to be fitted to were chosen by first simulating nine separate event lists and then choosing the one with the median number of counts, in order to avoid contaminating the verification process with extremal data sets. The fits were carried out as described in § 3.2, and the resulting best-fit values α_{FIT} are shown in Figure 6. The fitted values follow the true values closely for all three parameters.

The method works well over the range of interesting α , that is, spanning the value $\alpha = 2$, and is capable of distinguishing between sources with α above or below this critical value (see § 1). The sensitivity of the method naturally decreases as α increases to $\gtrsim 3$ when the data sets become indistinguishable from that of a steady source. However, this is not a hard limit and can be extended for data sets with larger average flare component intensity r_F and longer observations ΔT . The reliability also decreases as α decreases to $\lesssim 1.5$, since at these values of α , the simulations are dominated by a very few but very large flares and are therefore subject to large fluctuations and hence are not robust. A larger number of simulations at each grid point

¹⁰ Other well-known methods of summarizing probability distributions include noting the MAP (the mode of the distribution) as, e.g., $p(\alpha_{\text{MAP}}|D, I) = \max_{\alpha} \{p(\alpha|D, I)\}$, or a range corresponding to an integrated area under the curve, equivalent to some defined probability $\pi = \int_{\alpha_{\text{min}}}^{\alpha_{\text{max}}} p(\alpha|D, I)$, such that $\alpha_{\text{MAP}} \in [\alpha_{\text{min}}, \alpha_{\text{max}}]$, etc. Unless otherwise specified, we always report the mean values and 1σ errors.

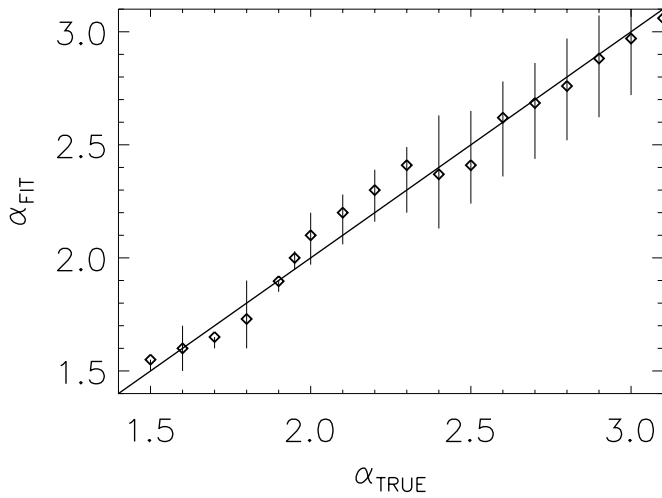


FIG. 6.—Verifying the method. The best-fit values α_{FIT} obtained for simulated data sets generated using a specific value α_{TRUE} are shown as diamonds, and the 90% credible regions are shown as vertical bars. The line of equality (solid line) is also shown.

becomes necessary when a data set exhibits smaller values of α .

3.3.2. Assumptions

We have made a number of simplifying assumptions in our analysis, and these are discussed below, with particular attention to the effect they have toward the robustness of the results. In general, all our assumptions are conservative, in the sense that they all act to generate a best-fit α and r_F that is smaller than the true α and r_F . That is, the main results expounded here—that the flare distributions on active stars have $\alpha > 2$ and that the apparently quiescent emission is dominated by flares—are not affected.

Power laws.—It has been well established that energy release due to flare events in both solar and stellar environments is highly intermittent and that the events are distributed as power laws spanning many decades in energy (e.g., Crosby et al. 1993; Güdel et al. 1997; Güdel 1997; Krucker & Benz 1998; Osten & Brown 1999; Audard et al. 2000; Aschwanden et al. 2000; Veronig et al. 2002). This suggests the absence of a characteristic scale for the intensity of a flare event and is understood to arise from avalanche or self-organized critical (SOC) models (Lu & Hamilton 1991; Vlahos et al. 1995; Georgoulis & Vlahos 1998; Krasnosel'skikh et al. 2001). Nevertheless, there is evidence from studies of solar flares that the index of the power-law distribution does not remain the same in the microflare and nanoflare range (cf. Aschwanden et al. 2000, their Fig. 10; Winebarger et al. 2002). Studies of stellar flares (e.g., Ambruster et al. 1987) also suggest that more than one type of plasma instability may be present and that the distribution may steepen or change at lower flare energies; for instance, compare $\alpha \approx 1.8$ found by Osten & Brown (1999) with the generally larger values found by Audard et al. (2000), who include much weaker flares in their analysis (also see the results from AD Leo presented here in § 4). Studies of flare distributions arising from the transition region also show a similar dichotomy (Robinson et al. 2001). Such changes in power-law indices could arise from a

variable driving mechanism (Georgoulis & Vlahos 1998). It is therefore possible that the true distribution departs from exact self-similarity in some complicated manner. However, present data, especially in the case of stellar flares, are insufficient to detect these departures (Audard et al. 1999, 2000; also Güdel et al. 2001, 2002). Here we assume that a single power-law index is valid over at least 4 orders of magnitude (see Table 4) in flare energy. If the distribution does steepen for lower flare intensities, then note that first, the steepest parts, which approach the limiting case of constant emission (see eq. [9a]), will contribute to enhancing the constant intensity r_C (as described in § 3.2). Hence, the fitted r_F is a lower limit to the true value. Second, the fitted α is a weighted average biased toward the high count rate, shallower distribution, and, inasmuch as a “true” value of α can be said to exist, it would be greater than the fitted value.

Decay timescales.—We analyze the data by fitting the three parameters α , r_F , and r_C of the model (eqs. [2a] and [2b]). We assume that the flare decay timescale τ (eq. [3b]) is fixed (usually at 3 ks, as suggested by the detectable flares and the radiative cooling timescales suggested by *ROSAT* observations; see, e.g., Giampapa et al. 1996) and is the same for all flares. However, it is well known that τ varies for individual flares on active stars (e.g., Pallavicini et al. 1990) and especially so for RS CVn stars (Osten & Brown 1999). Note, though, that we confine ourselves to a specific class of active stars—low-mass main-sequence stars that flare frequently—and exclude RS CVn stars from our sample. There is evidence that flare duration scales with flare energy in various passbands (e.g., Crosby et al. 1993; also, Vlahos et al. 1995 for avalanche models, Temmer et al. 2001 for H α flares, Georgoulis, Vilmer, & Crosby 2001 for decacV flares, Robinson et al. 2001 for chromospheric and transition region events, and Veronig et al. for *GOES* soft X-ray [SXR] flares), such that more intense flares appear to last longer. On the basis of avalanche model simulations, Lu et al. (1993) find that on average, an event with decay timescale τ corresponds to an energy release $E \propto \tau^{1.7}$. (See also the discussion below about sympathetic flaring, which could affect measurements of flare durations.) But note that the decay timescales for SXRs (such as the ones we are concerned with) are primarily dependent on flare temperature and plasma density, and secondary effects such as changes in the heating rate come into play only for very large flares in which the heating timescales approach or surpass the radiative cooling timescales. In a model that incorporates such variations of τ , the fainter flares will have larger peak rates than in the regular model (in order to have the same total energy output), and the distribution of arrival times $g(\delta t)$ will be skewed toward smaller δt . Thus, fitting to data that can be generated in this manner using a τ fixed by the higher intensity flares would result in $\alpha_{\text{FIT}} < \alpha_{\text{TRUE}}$ (see Fig. 5), and therefore the fitted values would be lower limits to the true indices. Conversely, fitting a model in which τ decreases with flare energy to a data set that is not generated in this manner will result in $\alpha_{\text{FIT}} > \alpha_{\text{TRUE}}$. (See also the discussion by Güdel et al. 2001, 2002.) In order to test the sensitivity of our data sets to these variations in modeling, we have carried out fits to the data using models with an energy-dependent timescale, $\tau \propto E^\beta$, in particular, $\beta = \frac{1}{4}$ (Güdel et al. 2002, based on fits to *EXOSAT* flare decay timescales of Pallavicini et al. 1990). We find that the best-fit value of α increases by ~ 0.3 – 0.4 for the complex model, e.g., for segment 3 of AD Leo α changes from 2.2 to 2.7. We

thus conclude that using the simpler model ($\tau = \text{constant}$) is preferable, in that we do not overestimate α , and further note that stronger dependences, e.g., that suggested by the theoretical study of Lu et al. (1993; $\tau \propto E^{0.56}$), would result in even larger fitted values of α . In addition, we have also explored the sensitivity of fits to the adopted value of τ , by generating simulated data with small decay timescales τ_{SIM} and then fitting to it a model with a larger decay timescale τ_{FIT} . We find that, as expected, the best-fit α is *smaller* than the true value, i.e., $\alpha_{\text{FIT}}|_{(\tau_{\text{FIT}} > \tau_{\text{SIM}})} < \alpha_{\text{SIM}}|_{\tau_{\text{SIM}}}$.¹¹ The reverse holds true for the opposite case, i.e., $\alpha_{\text{FIT}}|_{(\tau_{\text{FIT}} < \tau_{\text{SIM}})} > \alpha_{\text{SIM}}|_{\tau_{\text{SIM}}}$, in which case the best-fit values imply flare distributions that are steeper than they should be. Thus, the relatively large value we adopt for τ (3 ks) provides a conservative estimate, and the fitted values can be considered lower limits to the true values.

Rise times.—We model the flares as having an instantaneous rise and a slow exponential decay (eq. [3b]). In general, this is a good approximation, since the rise times are short compared to the flare duration (e.g., Reale, Peres, & Orlando 2001; Temmer et al. 2001). Further, our algorithm is insensitive to the exact sequence of the emission intensities [i.e., the process of forming $g(\delta t)$ destroys the sequential information in the event lists], and thus any discernible flare rise times will be indistinguishable in their effects from flares of small decay times. Thus, this approximation reduces to the problem discussed above, that of a sequence of flares that are “contaminated” by flares with smaller decay timescales, with similar effects on α and r_F .

Flare waiting times.—Much work has been done to characterize the time between flares within individual active regions. If we consider each flare to be an independent event, then the waiting time between flares is a Poisson process (Rosner & Vaiana 1978). However, actual observations of solar HXR flares show that the waiting-time distribution (WTD) is a power law in intervals, with index ranging from -2.16 to -2.4 (Boffetta et al. 1999; Wheatland 2000; Lepreti, Carbone, & Veltri 2001), although Moon et al. (2001) find that for strong solar flares (strength greater than C1), the waiting times are indeed well characterized by a Poisson distribution. The power-law distribution has been interpreted as due to sympathetic flaring (i.e., a cascade of small flares that follow a large flare, thus invalidating the assumption of event independence) by Wheatland, Sturrock, & McTiernan (1998) and adapted within SOC models as a nonstationary random process (Norman et al. 2001). However, since we can observe only disk-integrated flux in stellar data (it is not possible to monitor individual active regions), event independence is a better approximation. We thus assume in our modeling that the stellar flare WTD is Poisson. In such a case, the model undercounts the number of flares separated by short intervals (Wheatland et al. 1998). These flares would be generally associated with the stronger flares that set off a cascade, thus effectively increasing the decay timescale for large flares. As argued above, this causes $\alpha_{\text{FIT}} < \alpha_{\text{TRUE}}$.

¹¹ This effect is large only for small values of α . For example, $\{\alpha_{\text{SIM}} = 1.7; \tau_{\text{SIM}} = 1000\}$ is fitted by $\{\alpha_{\text{FIT}} = 1.5 \pm 0.02; \tau_{\text{SIM}} = 3000\}$, whereas $\{2.1; 500\}_{\text{SIM}}$ is fitted by $\{2.16 \pm 0.17; 3000\}_{\text{FIT}}$ (i.e., is indistinguishable from the true value), etc. Note that, as expected, this exercise also shows that when the data are dominated by multiple overlapping flare events, the results are insensitive to the precise value of the decay timescale, and effects such as stellar rotation may be ignored.

Energy deposition.—We have implicitly assumed that the observed counts track the energy deposited by the flares linearly (see eqs. [1] and [4]). That is, we assume that the energy deposition process that causes the flare event (generally considered to be magnetic reconnection—see Parker 1988) is, first, sufficiently energetic that a large fraction of the deposited energy goes toward thermal loading of the plasma and not into bulk motions (see Winebarger et al. 2002); second, that the resulting plasma temperatures for all flare energies lie near 10^7 K; and third, that the temperature evolution of the plasma after the flare event is not drastic. These assumptions are supported by the emission measure analysis of several *Yohkoh* flares by Reale et al. (2001), who find that solar flares are dominated by emission at ~ 10 mK. Hydrodynamic modeling of an ensemble of flaring loops by Güdel et al. (1997) and Güdel (1997) also shows that the bulk of the flare DEM lies above 6 mK; indeed, Güdel (1997) finds that the DEM is bimodal around 10 mK, attributable to the slightly smaller temperatures generated by the weaker flares (but which are still significantly hotter than the temperatures achieved by the quiet Sun). Thus, while it is reasonable to expect that flare emission would evolve from temperatures of ~ 20 to ~ 5 mK and that flare events that are less energetic would heat the plasma to a lower temperature, in practice the effects of such variations are very little. Furthermore, because we model the distribution in counts space, i.e., dN/dc rather than dN/dE directly, we invariably obtain distributions that are *shallower* than the true distributions¹² (see also extensive discussion in Güdel et al. 2002). In the *EUVE/DS*, changes in temperature of this magnitude cause the observed counts to vary by a factor of ≈ 2 . Furthermore, the range of flare energies we can model (see Table 4) is much larger than the relatively low-energy “explosive events” that are characterized by large nonthermal velocities (Winebarger et al. 2002 and references therein) and that may not contribute significantly to the plasma heating. That is, we assume that lower energy depositions that may heat the plasma to lower temperatures would not be detectable by the *EUVE/DS* in any case. Note that the assumed abundances will also affect this to some extent, but its effect is minimal for a broadband instrument such as is used here. We therefore assume that an observed *EUVE/DS* count corresponds to a photon of average energy 1.7×10^{-11} ergs cm^{-2} count^{-1} over the 59–250 Å range produced by a plasma at 10^7 K (PIMMS v2.5).

¹² Suppose we write the observed counts generated in a detector c_{obs} due to emitted energy E_{true} as a power law that deviates from linearity by a small amount, $c_{\text{obs}} \propto E_{\text{true}}^{1+\delta}$, $\delta > 0$. That is, as E_{true} decreases, the counts produced in the detector decrease at a faster than linear rate, as would be expected to happen if the lower energy flares result in lower plasma temperatures, and the detector has a smaller response to these temperatures. This is a reasonable approximation for broadband instruments such as the *EUVE/DS*, although it may not be applicable for small-passband detectors such as the *Transition Region and Coronal Explorer (TRACE)* (see Aschwanden & Charbonneau 2002). If $(dN/dE_{\text{true}}) \propto E_{\text{true}}^{-\alpha_{\text{true}}}$, then $(dN/dc_{\text{obs}}) \propto c_{\text{obs}}^{-\alpha_{\text{obs}}}$, where $\alpha_{\text{obs}} = (\alpha_{\text{true}} + \delta)/(1 + \delta)$, and is always smaller than α_{true} for $\delta > 0$ and $\alpha_{\text{true}} > 1$. Conversely, if $\delta < 0$, as may happen for extremely high-flare energies and temperatures that lie above the best response of the detector, the observed distribution will be steeper than the true distribution, $\alpha_{\text{obs}} > \alpha_{\text{true}}$; however, this case has little effect on our analysis results because of the wide temperature response of the *EUVE/DS*, and any flares that fall outside its range would be too few in number to affect the results.

Cutoffs.—We have adopted upper and lower limits to the extent of the power-law distribution (see eq. [5]) that are based strictly on numerical expediency: the upper limit is set by the requirement that the largest possible flare can produce no more than the observed number of counts, and the lower limit is defined by the minimum number of counts needed to define an interval. How do these limits compare with theoretical expectations? First, note that the solar flare distribution has been explored to much lower energies, $E \sim 10^{23}$ ergs (Winebarger et al. 2002), than have been achieved for stellar observations. Recently, Katsukawa & Tsuneta (2001) have estimated that the probable energy of Parker-type nanoflares is less than 10^{22} ergs. In contrast, we find that if the observed *EUVE* emission is assumed to originate entirely in flares, then it is sufficient to extend the power-law distributions to energies $E \sim 10^{28}$ – 10^{29} ergs (see Table 4). We suggest that the discrepancy is not due to a higher cutoff energy in the stellar case but rather that our analysis is physically limited because of a combination of the lack of instrument sensitivity, possible power-law changes, and systematic bias due to temperature effects in very small flares (see above). By modeling flares as driven dissipative avalanche systems, Lu et al. (1993) predict a high-energy rollover in the energy distribution whose magnitude depends on the size of the active region where the flares occur. Kucera et al. (1997) have applied this to *Solar Maximum Mission (SMM)*/hard X-ray burst spectrometer (HXRBS) data and find empirically that the total energy of an event has a maximum, $E_{\text{cutoff}} \approx 5 \times 10^{28} A_{\mu\text{hs}}^{5/4}$ ergs, where $A_{\mu\text{hs}}$ is the total area of active regions in units of solar microhemispheres, i.e., $1 \mu\text{hs} = 3.04 \times 10^{18}$ cm². Thus, for active stars such as the ones we are considering, in which active regions covering large fractions of the stellar surface are expected ($A_{\mu\text{hs}} \gg 10^4$), total flare energies in excess of 10^{33} ergs are achievable, and thus our analyses are valid up to these energies.

Background corrections.—All the stars in our sample are strong sources of EUV emission, and the background is generally small compared to the source strength. We do not subtract the background from the data sets nor model it separately, but we assume that the constant component in the flare model (eq. [3a]) includes contamination due to the background. That is, we assume that the background does not vary on timescales smaller than the adopted decay timescale and that any variations that exist in the instrumental and astrophysical background are small in magnitude and do not contribute to the flare component. Any departures from strict constancy in the background will result in a poorer determination of r_C because of the larger spread in the distribution of arrival times, $g(\delta t)$ (see Fig. 5). In cases in which the above assumptions are invalid, the background data will contaminate the signal, but as estimated in Tables 1–3, this contamination will be $\lesssim 10\%$.

3.3.3. Advantages and Disadvantages

Unlike previous methods that determine flare number distributions nonparametrically, that is, by directly counting the number of detected flares, we *model* the flare distribution as a power law and generate photon arrival times to compare with the observed event lists. Thus, the validity of our results is directly dependent on the applic-

ability of the model (see extensive discussion in § 3.3.2), i.e., the derived parameter values are only as good as the model. Thus, our results are correct, subject to the caveat that we require that all flares are physically “similar” and that the flare distribution follows a power law. But the fact that we model the distribution means that we can usefully extend the analysis to the regime in which the light curves are dominated by large numbers of small undetectable flares, and hence this method is best suited to study continuous microflaring.

Because the model is stochastic in nature, any realization of the photon arrival times can be significantly different from the observed event list, even if the parameter set matches exactly. Thus, a large number of simulations must be carried out for each set of parameters, which is a time-consuming process. On the other hand, the stochastic nature of the model renders unnecessary an exact match between the model realization and the observed light curve, allowing us to explore weak flare events.

As shown in §§ 3.2 (Fig. 5) and 3.3.1, the method loses sensitivity for $\alpha \gtrsim 3$ and loses stability for $\alpha \lesssim 1.5$. However, over the range of α that is of scientific interest, i.e., spanning the critical value $\alpha = 2$, the method is robust and can discriminate between the two cases in which flare emission may be a significant contributor to the coronal emission budget ($\alpha > 2$) or in which the light curve may be dominated by large flares that do not contribute significantly to the energy budget ($\alpha < 2$).¹³

4. RESULTS

We have applied the algorithm detailed above (§ 3) to *EUVE*/DS data on FK Aqr, V1054 Oph, and AD Leo (see § 2). The results are summarized in Table 4. Below we comment on each data set in detail.

4.1. FK Aqr

As anticipated above (see Fig. 5), the maximum a posteriori (MAP) values (see footnote 10) for FK Aqr are $\alpha_{\text{MAP}} \approx 2.5$, $r_{F,\text{MAP}} \approx 0.22$, and $r_{T,\text{MAP}} \approx 0.36$, corresponding to a flare contribution of $\approx 65\%$ to the total emission. The joint probability distribution of α and r_F , marginalized over r_T , is shown in Figure 7, and the individual probability distributions of α and r_F , marginalized over the other parameters, are shown in Figure 8. The best-fit values are $\alpha = 2.60 \pm 0.34$, $r_F = 0.19 \pm 0.12$, and $r_T = 0.37 \pm 0.01$. The correlations between the parameters are evident in $p(\alpha, r_F)$. Note that there is a small probability (~ 0.1) that $\{r_F \ll r_T \text{ and } \alpha < 2\}$. It is worth pointing out the cause of the large values of the probability for small r_F . First, note the presence of a secondary peak at $(\alpha = 2.2, r_F = 0.05)$, which contributes to a larger spread in the uncertainty in r_F and, incidentally, also indicates the potential existence of multiple power-law components. Second, this effect is a measure of the stability of the model best-fit parameters to the data; if there are large parts of the parameter space that

¹³ Note that the mere fact that $\alpha > 2$ does not guarantee that the coronal emission is dominated by flaring, but the normalization of the power-law distribution must also be large. Our approach allows us to independently determine the flare contribution r_F to the total count rate. The results (see § 4) show that the normalization is such that the flare contribution is generally greater than 50%.

TABLE 4
SUMMARY OF RESULTS

Star	$\bar{\alpha}^a$	Flares ^b (%)	κ^c	E_{range}^d $\log_{10}(\text{ergs s}^{-1})$	E_{min}^e ($\times 10^{28}$ ergs)
FK Aqr.....	2.60 ± 0.34	~ 50 (65)	2.09×10^4	29.48–33.54	9.87
V1054 Oph.....	2.74 ± 0.35	70 (85)	8.6×10^3	29.12–32.67	8.64
AD Leo:					
[2, 3].....	2.17 ± 0.03	80 (80)	2.12×10^4	28.99–33.66	8.20
[4, 5].....	2.32 ± 0.11	65 (75)	2.8×10^4	28.99–33.52	3.40

^a Power-law index.

^b For the average rate, \bar{r}_F as a percentage of the average total rate; within brackets, for the mode $r_{F_{\text{MAP}}}$.

^c Normalization factor for power-law distribution, for best-fit parameters (see eq. [6a]).

^d Range of flare energies included in calculations (see eq. [5]).

^e Minimum flare energy to which a power law should be extended in order for the flare component to account for the entire emission.

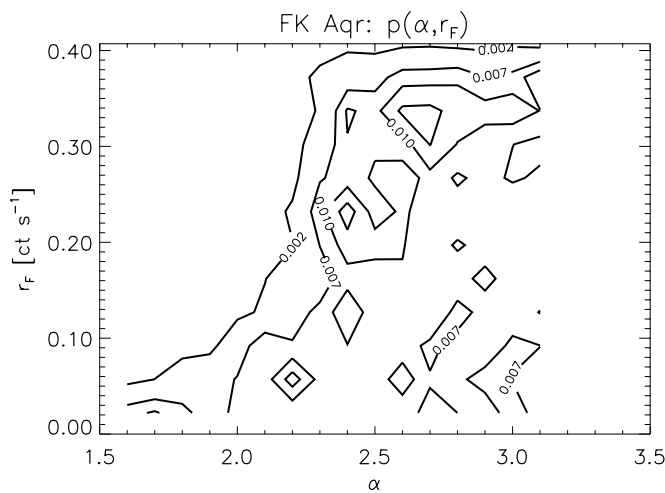


FIG. 7.—Joint posterior probability distribution of α and r_F , marginalized over r_T , for FK Aqr. The peak of the distribution lies at $\alpha_{\text{MAP}} = 2.5$ and $r_{F_{\text{MAP}}} = 0.22$.

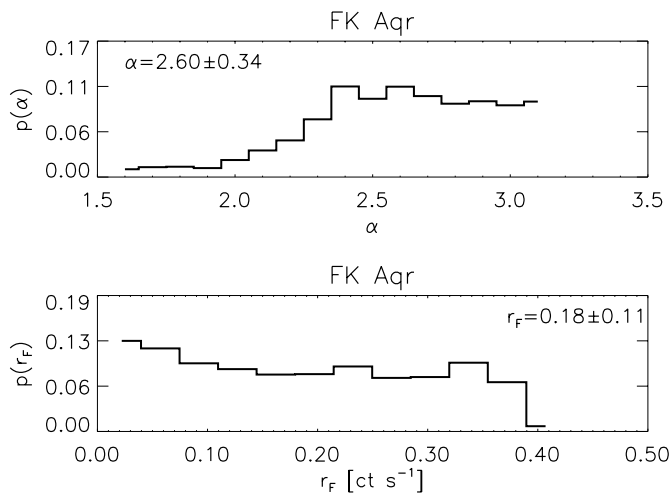


FIG. 8.—Marginalized one-dimensional posterior probability distributions of α and r_F for FK Aqr. Note the apparently large contribution at small r_F , which is a consequence of the fact that the flare contribution is poorly determined but cannot be ruled out for any α for small values of r_F .

provide adequate (although not good) fits to the data, their contributions are enhanced because of the larger volume of the space they occupy. This is indeed the case here for combinations of small values of r_F and α , in which the skewness induced in $g_{\text{MODEL}}(\delta t)$ by $\alpha < 2.5$ is minimized as a result of the lower weight accorded to it because of the smaller values of κ . Data from *Chandra* or *XMM-Newton*, with their higher expected count rates, are necessary to explore the region of smaller values of δt and thus better constrain the parameter ranges.

4.2. V1054 Oph

The light curve of V1054 Oph (Fig. 2) shows considerable variability with some relatively weak flarelike events. This is a signature of a flare distribution with large values of α , and indeed detailed analysis (see Figs. 9 and 10) confirms this impression; we find $\bar{\alpha} = 2.74 \pm 0.35$, with an upper bound that is not well constrained (Fig. 10). From the joint probability distribution $p(\alpha, r_F)$, the most probable values are $\alpha_{\text{MAP}} \approx 2.5$ and $r_{F_{\text{MAP}}} \approx 0.065$, suggesting that it is likely that almost all the observed emission originates in flarelike events (Fig. 9).

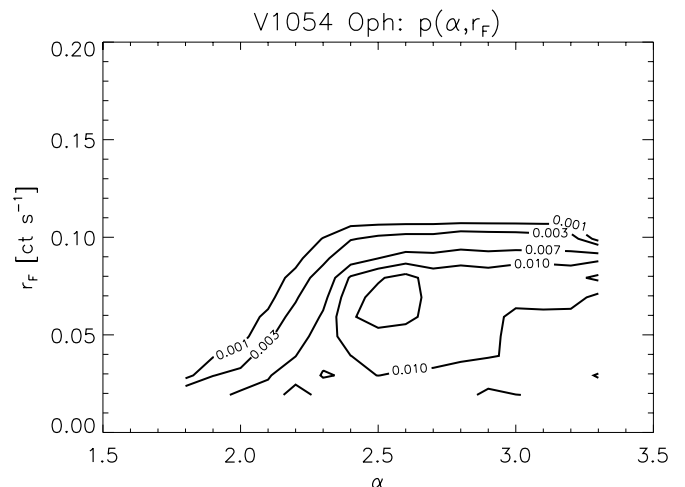


FIG. 9.—Same as Fig. 7 but for V1054 Oph

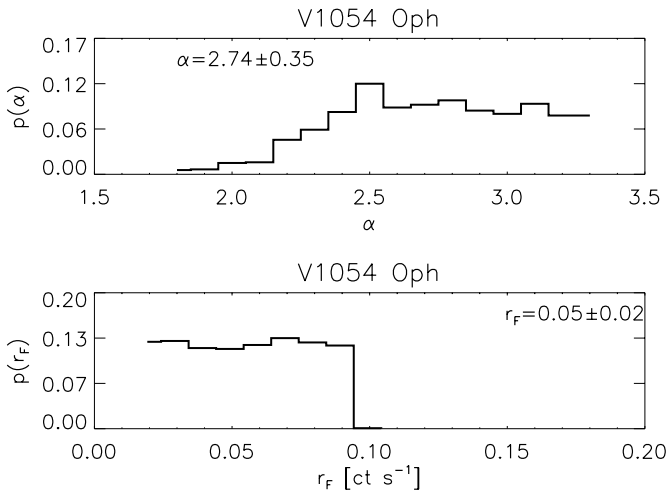


FIG. 10.—Same as Fig. 8 but for V1054 Oph. Note that there is significant mass in the distribution $p(\alpha)$ for large values of α , which implies that the upper bound is not well constrained. However, the lower bound is well determined to be $\gtrsim 2.2$.

4.3. AD Leo

In general, the AD Leo data have been analyzed in two separate batches because of the large time intervals and large number of counts involved (which leads to very long computation times) and also because the character of the light curve (see Fig. 3) appears to change from being dominated by an intense flare at the beginning (segments II+III) to being steadier, with weaker flare events (segments IV+V). The light curves also suggest that the flare distribution is characterized by smaller values of α than are FK Aqr and V1054 Oph. Detailed analysis confirms the latter, with $\overline{\alpha_{\text{II+III}}} = 2.17 \pm 0.03$ and $\overline{\alpha_{\text{IV+V}}} = 2.31 \pm 0.11$ (see Figs. 11 and 12), but the distributions $p(\alpha)$ overlap for the two segments, and we cannot rule out at the 10% confidence level that the α are identical for the two data sets. However, the trend for the analyses of individual segments ($\overline{\alpha_{\text{II}}} = 2.03 \pm 0.05$, $\overline{\alpha_{\text{III}}} = 2.22 \pm 0.07$, $\overline{\alpha_{\text{IV}}} = 2.21 \pm 0.06$, and $\overline{\alpha_{\text{V}}} = 2.31 \pm 0.03$) does suggest a gradual steepening of

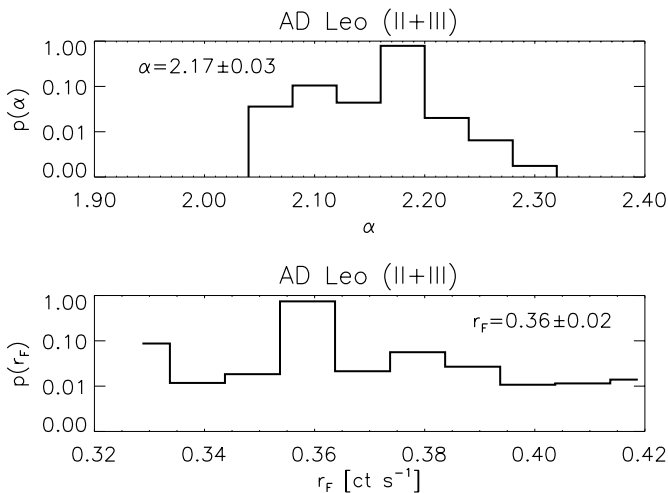


FIG. 11.—Same as Fig. 8 but for segments 2 and 3 of AD Leo. The parameters are well determined because of the large size of the data set. Values of $\alpha < 2$ can be emphatically ruled out.

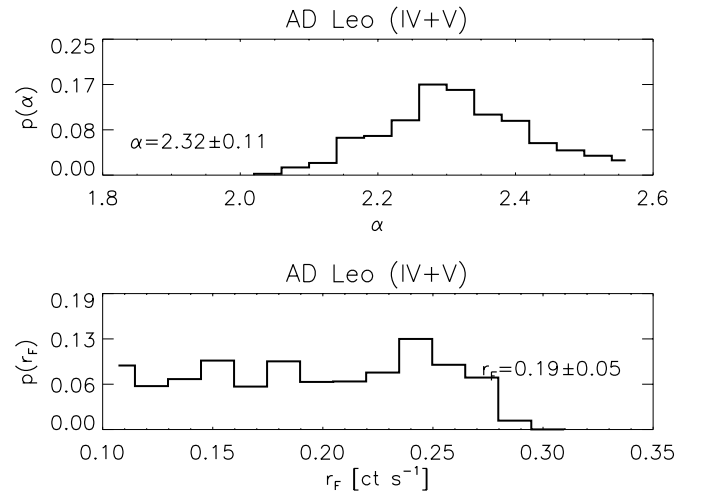


FIG. 12.—Same as Fig. 11 but for segments 4 and 5 of AD Leo. The best-fit value of α is larger than for segments 2 and 3, although the probability distributions do overlap. The relatively large spread in r_F is due to the larger allowed spread in α compared to the earlier data. The most probable values are $\alpha_{\text{MAP}} = 2.3$ and $r_{F\text{MAP}} = 0.24$, which implies that the data are almost entirely due to flaring emission.

the flare distribution when large flares are absent from the data set.

5. SUMMARY

We have modeled the event arrival times from active stars FK Aqr, V1054 Oph, and AD Leo, with particular attention to the component that arises from flarelike events. On the Sun, flares are known to be distributed as a power law in energy (Hudson 1991; also see Aschwanden et al. 2000 and references therein), and numerous studies have established that strong stellar flares also follow a power-law distribution, with indices ranging from 1.5 to 2.5 (see Audard et al. 2000 and references therein). This is of considerable interest, because if the power-law index α is greater than 2, then the coronal X-ray losses could in principle be ascribed to weak flare events that are nevertheless numerous enough to dominate the emission.

We consider active dMe stars with known variability in their light curves where numerous flares are seen. Audard et al. (2000) find that in general, dF and dG stars tend to have $\alpha > 2$, while dK and dM stars tend to have lower α . In particular, they analyze an older data set of AD Leo (from 1996 May) and show that detectable flares have $\alpha \in [1.18, 2.35]$ or $\alpha = 2.02 \pm 0.28$ using different methods. A more detailed analysis by Güdel et al. (2002) based on a larger sample of the data set used here shows $2.0 < \alpha < 2.5$.

We model the event arrival times using a simple two-component model composed of a constant rate component and a statistical ensemble of flare components, with the flare energies distributed as a power law. In general, the simplifying assumptions that we make (e.g., constancy of decay timescales, ignoring the rise times, assuming a constant counts-to-energy conversion factor, including the background directly in the model, etc.) are conservative and tend to underestimate the value of α . We find that all the stars in our sample clearly have $\alpha > 2$: for AD Leo, α lies in the range 2.06–2.32; for FK Aqr, $\alpha = 2.60 \pm 0.34$; and for V1054 Oph, $\alpha = 2.74 \pm 0.35$. We thus conclude that coro-

nal heating on these stars is dominated by impulsive energy release events whose energy output is $\gtrsim (2-3) \times 10^{29}$ ergs, reaching to the microflare range. These results are in contrast to the solar case, in which over similar flare energy ranges the observed distribution of flares is shallower, with $\alpha \approx 1.8$, i.e., below the critical value of 2.

Further, we directly estimate the contribution of the flare emission to the total observed count rate, as one of the parameters defining the model. Because the energy range over which the model is defined spans over 4 orders of magnitude, and the power-law indices indicate steep distributions, we expect that the flare component should contribute significantly to the total emission. Indeed, we find this to be generally greater than 50% and in some cases greater than 80%. Thus, there appears to be no truly “quiescent” emission on some of these low-mass active stars, i.e., emission from apparently stable active region loops as on the Sun is not a dominant component of the observed emission.

We also have explored the possible dependence of the various model parameters on flare energies. The long observation of AD Leo suggests that α increases when strong flares are not evident in the data, suggesting that the flare distribution steepens for flares of smaller energies, although we cannot rule out the possibility of a statistical fluctuation that mimics this trend. We also have searched for, but do not find, evidence of strong dependence of the decay time-scale on flare energies.

We find that if the flare distributions extend to the microflare regime, the energy output due to these weak flares is

quite sufficient to account for the entire coronal emission in the *EUVE/DS* passband. However, it must be noted that the error bars on the parameters derived for the fainter stars FK Aqr and V1054 Oph are quite large (for instance, values of $\alpha < 2$ cannot be completely ruled out for FK Aqr, and a firm upper bound on α cannot be set for V1054 Oph), and it would be of considerable interest to verify and improve these results (and also to extend them to a larger sample of stellar types) using high-quality data such as those obtainable with *Chandra* and *XMM-Newton*. Data from these observatories are characterized by good time resolution and in general larger count rates and will therefore allow us to explore the arrival-time difference distribution functions $g(\delta t)$ at smaller values of δt , thereby extending the range of values of α that the method is sensitive to.

We would like to thank David van Dyk, Alanna Connors, Eric Kolaczyk, and Olivia Johnson for useful discussions. We also thank the referee, J. Linsky, for valuable comments that improved the paper. V. L. K. was supported by NASA grants and the *Chandra* X-Ray Center during the course of this research. J. J. D. was supported by the *Chandra* X-Ray Center NASA contract NAS8-39073. The PSI group acknowledges support from the Swiss National Science Foundation (grants 2100-049343 and 2000-058827). This research has made use of the SIMBAD database, operated at Centre de Données Astronomiques de Strasbourg (CDS), Strasbourg, France.

APPENDIX

TABLE A1
GLOSSARY OF TERMS

Symbol	Description	First Use
$\Gamma(x)$	The gamma function, which for integer x is $(x - 1)!$	§ 3.2, eq. (10)
ΔT	Total duration of observation	§ 3.1, eq. (3c)
$\Theta(\cdot)$	Heaviside step function	§ 3.1, eq. (3b)
α	Power-law index	§ 1, eq. (1)
δt	Arrival-time difference between two consecutive photons	§ 3.2
κ	Normalization of the power law in counts units	§ 3.1, eq. (4)
$\phi(t)$	Instrument correction factor that includes Primbsching, etc.	§ 3.1, eq. (3a)
ρ_i	The fraction of time a source spends at rate r_i	§ 3.2, eq. (9b)
τ	Flare decay timescale	§ 3.1, eq. (3b)
χ^2	$= \sum_i \left[\frac{\text{Data}_i - \text{Model}_i}{\text{error}(\text{Data}_i)} \right]^2$, a statistic measuring the quality of a fit	§ 3.2, Fig. 5
$C(t)$	Model light curve, observable counts in $[t, t + dt]$	§ 3.1, eq. (3a)
D	Observed data	§ 3.2, eq. (7a)
E	Energy output of flare event	§ 1, eq. (1)
F_j	Peak intensity of model flare j	§ 3.1, eq. (3b)
\mathbf{M}, \mathbf{M}'	Set of parameters defining the model	§ 3.1, eqs. (2a) and (2b)
N_f	Total number of flares in the model	§ 3.1, eq. (3b)
I	Information necessary to define the problem	§ 3.2, eq. (7a)
dN	Number of flare events in $[E, E + dE]$	§ 1, eq. (1)
c	Counts due to a flare	§ 3.1, eq. (4)
c_{\max}	Maximum model counts possible because of a flare, for a given data set	§ 3.1, eq. (5)
c_{\min}	Minimum model counts due to a flare that is practicable to consider	§ 3.1, eq. (5)
$f(t)$	Flare model light curve intensity at time t	§ 3.1, eq. (3b)
$g(\delta t)$	Frequency histogram of the distribution of δt	§ 3.2, eq. (9a)
k	Normalization of the power law in energy units	§ 3.1, eq. (6a)
$p(A B)$	Probability that statement A is true, given that statement B is true	§ 3.2, eq. (7a)
$r(t)$	Model light-curve intensity	§ 3.1, eq. (3a)
r_C	Constant component model count rate	§ 3.1, eq. (2a)
r_F	Mean model count rate of flare component over duration of observation	§ 3.1, eq. (2a)
r_T	Mean total model count rate over duration of observation	§ 3.1, eq. (2b)
$\text{var}(x)$	Variance of quantity x	§ 3.2, eq. (12a)
\bar{x}	Mean value of quantity x	§ 3.2, eq. (12a)
x_{MAP}	Maximum a posteriori value of x , where $p(x)$ is maximum	§ 3.2, footnote 10

NOTE.—Here we compile, for reference, all the symbols used in the text.

REFERENCES

- Ambruster, C. W., Sciortino, S., & Golub, L. 1987, *ApJS*, 65, 273
 Aschwanden, M. J., & Charbonneau, P. 2002, *ApJ*, 566, L59
 Aschwanden, M. J., & Parnell, C. E. 2002, *ApJ*, 572, 1048
 Aschwanden, M. J., Tarbell, T. D., Nightingale, R. W., Schrijver, C. J., Title, A., Kankelborg, C. C., Martens, P., & Warren, H. P. 2000, *ApJ*, 535, 1047
 Audard, M., Güdel, M., Drake, J. J., & Kashyap, V. L. 2000, *ApJ*, 541, 396
 Audard, M., Güdel, M., & Guinan, E. F. 1999, *ApJ*, 513, L53
 Benz, A. O., & Güdel, M. 1994, *A&A*, 285, 621
 Boffetta, G., Carbone, V., Giuliani, P., Veltri, P., & Vulpiani, A. 1999, *Phys. Rev. Lett.*, 83, 4662
 Butler, C. J., Rodono, M., Foing, B. H., & Haisch, B. M. 1986, *Nature*, 321, 679
 Byrne, P. B., Butler, C. J., & Lyons, M. A. 1990, *A&A*, 236, 455
 Cheng, C.-C., Doschek, G. A., & Feldman, U. 1979, *ApJ*, 227, 1037
 Collura, A., Pasquini, L., & Schmitt, J. H. M. M. 1988, *A&A*, 205, 197
 Crawford, D. F., Jauncey, D. L., & Murdoch, H. S. 1970, *ApJ*, 162, 405
 Crosby, N. B., Aschwanden, M. J., & Dennis, B. R. 1993, *Sol. Phys.*, 143, 275
 Dempsey, R. C., Linsky, J. L., Schmitt, J. H. M. M., & Fleming, T. A. 1993, *ApJ*, 413, 333
 Doyle, J. G., & Butler, C. J. 1985, *Nature*, 313, 378
 Drake, J. J. 1996, in *ASP Conf. Ser. 109, Cool Stars, Stellar Systems, and the Sun*, ed. R. Pallavicini & A. K. Dupree (San Francisco: ASP), 203
 Eadie, W. T., Drijard, D., James, F. E., Roos, M., & Sadoulet, B. 1971, *Statistical Methods in Experimental Physics* (Amsterdam: North-Holland)
 Georgoulis, M. K., Vilmer, N., & Crosby, N. B. 2001, *A&A*, 367, 326
 Georgoulis, M. K., & Vlahos, L. 1998, *A&A*, 336, 721
 Giampapa, M. S., Rosner, R., Kashyap, V., Fleming, T. A., Schmitt, J. H. M. M., & Bookbinder, J. A. 1996, *ApJ*, 463, 707
 Güdel, M. 1997, *ApJ*, 480, L121
 Güdel, M., Audard, M., Guinan, E. F., Drake, J. J., Kashyap, V. L., Mewe, R., & Alekseev, I. Y. 2001, in *ASP Conf. Ser. 234, X-Ray Astronomy 2000*, ed. R. Giacconi, L. Stella, & S. Serio, in press (astro-ph/0011572)
 Güdel, M., Audard, M., Kashyap, V. L., Drake, J. J., & Guinan, E. F. 2002, *ApJ*, submitted
 Güdel, M., & Benz, A. O. 1993, *ApJ*, 405, L63
 Güdel, M., Guinan, E. F., & Skinner, S. L. 1997, *ApJ*, 483, 947
 Hudson, H. S. 1991, *Sol. Phys.*, 133, 357
 Kashyap, V., & Drake, J. J. 1998, *ApJ*, 503, 450
 Kashyap, V., Rosner, R., Harnden, F. R., Jr., Maggio, A., Micela, G., & Sciortino, S. 1994, *ApJ*, 431, 402
 Katsukawa, Y., & Tsuneta, S. 2001, *ApJ*, 557, 343
 Kellett, B. J., & Tsikoudi, V. 1999, *MNRAS*, 308, 111
 Kopp, R. A., & Poletto, G. 1993, *ApJ*, 418, 496
 Krasnoselskikh, V., Podladchikova, O., Lefebvre, B., & Vilmer, N. 2001, *A&A*, submitted (astro-ph/0104241)
 Krucker, S., & Benz, A. O. 1998, *ApJ*, 501, L213
 Kucera, T. A., Dennis, B. R., Schwartz, R. A., & Shaw, D. 1997, *ApJ*, 475, 338
 Lepreti, F., Carbone, V., & Veltri, P. 2001, *ApJ*, 555, L133
 Lin, R. P., Schwartz, R. A., Kane, S. R., Pelling, R. M., & Hurley, K. C. 1984, *ApJ*, 283, 421
 Lored, T. J. 1990, in *Maximum Entropy and Bayesian Methods*, ed. P. F. Fougere (Dordrecht: Kluwer), 81
 Lu, E. T., & Hamilton, R. J. 1991, *ApJ*, 380, L89

- Lu, E. T., Hamilton, R. J., McTiernan, J. M., & Bromund, K. R. 1993, *ApJ*, 412, 841
- Moon, Y., Choe, G. S., Yun, H. S., & Park, Y. D. 2001, at AGUSP, Waiting-Time Distribution and Angular Correlation Function of Solar X-Ray Flares, #SP41A-01 (Washington: AGU)
- Narain, U., & Ulmschneider, P. 1990, *Space Sci. Rev.*, 54, 377
- . 1996, *Space Sci. Rev.*, 75, 453
- Norman, J. P., Charbonneau, P., McIntosh, S. W., & Liu, H.-L. 2001, *ApJ*, 557, 891
- Osten, R., & Brown, A. 1999, *ApJ*, 515, 746
- Pallavicini, R., Tagliaferri, G., & Stella, L. 1990, *A&A*, 228, 403
- Parker, E. N. 1988, *ApJ*, 330, 474
- Parnell, C. E., & Jupp, P. E. 2000, *ApJ*, 529, 554
- Perryman, M. A. C., et al. 1997, *A&A*, 323, L49
- Porter, J. G., Fontenla, J. M., & Simnett, G. M. 1995, *ApJ*, 438, 472
- Reale, F., Peres, G., & Orlando, S. 2001, *ApJ*, 557, 906
- Robinson, R. D., Carpenter, K. G., & Percival, J. W. 1999, *ApJ*, 516, 916
- Robinson, R. D., Carpenter, K. G., Percival, J. W., & Bookbinder, J. A. 1995, *ApJ*, 451, 795
- Robinson, R. D., Linsky, J. L., Woodgate, B. E., & Timothy, J. G. 2001, *ApJ*, 554, 368
- Rosner, R., Golub, L., & Vaiana, G. S. 1985, *ARA&A*, 23, 413
- Rosner, R., & Vaiana, G. S. 1978, *ApJ*, 222, 1104
- Schrijver, C. J., et al. 1999, *Sol. Phys.*, 187, 261
- Shimizu, T. 1995, *PASJ*, 47, 251
- Shimizu, T., & Tsuneta, S. 1997, *ApJ*, 486, 1045
- Skumanich, A. 1985, *Australian J. Phys.*, 38, 971
- Stepien, K., & Ulmschneider, P. 1989, *A&A*, 216, 139
- Strassmeier, K. G., Hall, D. S., Fekel, F. C., & Scheck, M. 1993, *A&AS*, 100, 173
- Temmer, M., Veronig, A., Hanslmeier, A., Otruba, W., & Messerotti, M. 2001, *A&A*, 375, 1049
- van Dyk, D., Connors, A., Kashyap, V. L., & Siemiginowska, A. 2001, *ApJ*, 548, 224
- Veronig, A., Temmer, M., Hanslmeier, A., Otruba, W., & Messerotti, M. 2002, *A&A*, 382, 1070
- Vlahos, L., Georgoulis, M., Kluiving, R., & Paschos, P. 1995, *A&A*, 299, 897
- Wheatland, M. S. 2000, *ApJ*, 536, L109
- Wheatland, M. S., Sturrock, P. A., & McTiernan, J. M. 1998, *ApJ*, 509, 448
- Winebarger, A., Emslie, A. G., Mariska, J. T., & Warren, H. P. 2002, *ApJ*, 565, 1298